materials

MDPI

Article

Hot Corrosion Behavior and Damage Mechanism on Yield Property of Nickel-Based Superalloy

Xinyu Meng [1,2], Shaomin Lyu [2,3,*], Xingfei Xie [2,3], Chao Tang [2,3], Wugang Yu [4], Weixue Hou [2,3], Chengyu Wang [2,3], Jinglong Qu [2,3,*] and Jinhui Du [2,3]

[1] Research Institute of High-Temperature Materials, Central Iron and Steel Research Institute Co., Ltd., Beijing 100081, China
[2] Beijing GAONA Materials and Technology Co., Ltd., Beijing 100081, China; superalloy_1@163.com (J.D.)
[3] Sichuan CISRI-GAONA Forging Co., Ltd., Deyang 618000, China
[4] NCS Testing Technology Co., Ltd., Beijing 100081, China
* Correspondence: lsmleon@163.com (S.L.); qujinglong@cisri.cn (J.Q.)

Abstract: Ni-based superalloys with enhanced environmental resistance at high temperatures are crucial for advanced gas turbine engines. The new polycrystalline nickel-based superalloy has excellent mechanical properties, but as a low-Cr, high-alloying superalloy, its environmental resistance has never been investigated. The hot corrosion behavior of the nickel-based superalloy under molten salt conditions and its effect on its tensile properties were investigated in this paper. The results showed the following: The diffusion of the Cr, Al, and Ni elements governs the majority of the corrosion process, resulting in the production of an environmentally damaged organization with internal sulfidation and surface oxidation. The Wagner model predicts the inability to form a dense Al oxide scale on the surface because the crucial generation condition of external Al oxides is not met. In addition, the growth stress in the damage scales is the main cause of cracking and spalling in the isothermal corrosion process. Due to the increased local stress concentration brought on by this environmental degradation, the sulfide scale acts as a fracture source, guiding the matrix cracking and influencing the tensile properties of the alloy.

Keywords: nickel-based superalloy; hot corrosion behavior; microstructure evolution; damage mechanism; tensile properties

check for updates

Academic Editor: Gábor Harsányi

Received: 11 February 2025
Revised: 23 February 2025
Accepted: 26 February 2025
Published: 11 April 2025

Citation: Meng, X.; Lyu, S.; Xie, X.; Tang, C.; Yu, W.; Hou, W.; Wang, C.; Qu, J.; Du, J. Hot Corrosion Behavior and Damage Mechanism on Yield Property of Nickel-Based Superalloy. *Materials* **2025**, *18*, 1749. https://doi.org/10.3390/ma18081749

Copyright: © 2025 by the authors. Licensee MDPI, Basel, Switzerland. This article is an open access article distributed under the terms and conditions of the Creative Commons Attribution (CC BY) license (https://creativecommons.org/licenses/by/4.0/).

1. Introduction

A superalloy refers to a material able to withstand large complex stresses at high temperatures above 600 °C and that has the surface stability of high-alloyed iron-based, nickel-based, or cobalt-based austenitic metal materials. Nickel-based superalloys refer to materials with high-alloyed nickel-based austenite as a substrate or nickel as the main element, as well as nickel–aluminum intermetallic compounds to produce high-temperature materials. Because of their superior fatigue and creep resistance, excellent high-temperature ductility, and strong resistance to oxidation and corrosion, nickel-based superalloys have emerged as the preferred material for critical aerospace engine components like turbine disks [1]. They occupy about 30–40% of the global aerospace engine material market. In addition, their market share in the non-aerospace sector is about 20–30%. Nickel-based superalloys contribute significantly to economic growth, and market demand is expected to continue to rise at a compound annual growth rate of 3–5%, with promising prospects for future development. Dynamic advancements in aero-engine technology have led to a heightened demand for an improved engine thrust-to-weight ratio, thermal efficiency, and

service life. As a result, higher standards for the service temperature, high-temperature mechanical characteristics, and stability of superalloys have been established for turbine disks [2,3]. Advanced nickel-based superalloys are used in environments with temperatures higher than 700 °C. Since these alloys are used as hot-section components in aircraft applications that are exposed to fuel oil, oxidation, and marine atmospheric air streams, it will be interesting to see how they respond to environmental damage in the future. At this stage, by precisely controlling the nanomechanical properties of the material, the microstructure can be indirectly regulated, and the closure of micropores or the expansion of cracks can be observed by selecting different working conditions [4]. By optimizing the microstructure of the coating and reducing the formation of micropores and cracks, the hardness and abrasion resistance of the nickel-based gradient coating can be significantly improved, which provides a basis for the optimal design of the material [5]. Despite the fact that thermal barrier coatings, which are currently the main defense against high temperatures, can greatly extend service life [6], there are problems like coating–substrate thermal expansion mismatch, which can cause the coating or oxide scale to crack and spall, leading to failures [7,8]. Consequently, in order to quantify and regulate their mechanical properties during the service process, a thorough investigation of the environmental damage mechanism of the nickel-based superalloy material and a clarification of its impact on these mechanical properties is necessary. Following this, the environmental damage mechanism of the alloy must be predicted.

The deep and protective oxide scales of chromium (III) oxide (Cr_2O_3) and aluminum oxide (Al_2O_3) are primarily responsible for the exceptional resistance to environmental degradation exhibited by nickel-based superalloys [9]. Furthermore, the elements of chromium (Cr) and aluminum (Al) can slow down the rate of oxidation and hot corrosion [10,11]. Typically, nickel-based superalloys exhibit a very complex element diffusion behavior upon applied loads, which is caused by the environmental damage that occurs at high temperatures [10]. Although nickel-based superalloys can form protective oxides to enhance their corrosion resistance, the depletion of surface/near-surface alloying elements such as Cr, Al, and titanium (Ti) leads to the degradation of their properties, crack initiation, and fatigue failure [12,13]. The combination of temperature and stress can also lead the protective scale to break or be destroyed and can further oxidize and corrode the material [14–16]. Because of the higher service temperature of wrought superalloys, precipitation-strengthening elements are elevated, but solution-strengthening elements such as Cr are relatively low. Little research has investigated the environmental damage of low-Cr-content superalloys under service conditions at the maximum temperature of turbine disks. The structural changes in these alloys during the steady-state hot corrosion process, as well as the effect of the changes on the mechanical properties of the alloy, have never been investigated.

In order to study the hot corrosion mechanism of superalloys, researchers from both domestic and foreign universities currently use a certain mass fraction ratio of mixed salt Na_2SO_4 + NaCl for hot corrosion in crucibles and other containers covering the alloy surface. Mahobia et al. [17] found that the accompanying sulfur (S) element causes the sulfidation of Inconel 718 and GH4169 acicular δ-phase (Ni_3Nb) and enrichment within the corrosion scale. According to research by Wei et al. [18], S can infiltrate the Cr_2O_3 oxide scale created by Inconel 600, diffuse into the matrix along grain boundaries, and mix with Cr to generate sulfide, which weakens the intergranular bond strength. However, S and nickel (Ni) in the alloy matrix combine to generate the low-melting-point compound nickel (II) sulfide (Ni_3S_2), which continuously melts when used and eventually causes sulfidation corrosion to develop. Birbilis et al. [19] used the XPS method to show that Rene104 has a rising amount of sulfur-containing compounds because there is not enough chromium

oxide on the surface of the alloy during hot corrosion and that sulfur-related corrosion determines the damage. According to research by Nazmy [20] and others, the impact of sulfidation on the crack initiation process is responsible for the decrease in the LCF life of the IN738 alloy when exposed to synthetic ash and air containing sulfur dioxide/sulfur trioxide (SO_2/SO_3) at 850 °C-1000 h. Additionally, the fatigue behavior is impacted by anti-pitting and internal sulfidation that occur at the front of corrosion pits due to the erosive form of hot corrosion [21]. However, current research on superalloys under hot corrosion conditions mainly focuses on isothermal hot corrosion behavior, with less research on oxidation behavior and elemental competition mechanisms during the corrosion process. The effect of the evolution of the damaged organization on the mechanical properties during isothermal hot corrosion remains to be studied. An experimental alloy, as a high-alloying superalloy, will have a damaged structure and element diffusion mechanism that will be more complicated during the environmental damage process. Therefore, further study of the environmental damage mechanism and its effect on properties is necessary to promote the optimization of the alloy composition.

It is the first work to investigate the isothermal hot corrosion test of the alloy at 700–800 °C in molten salt of 75% Sodium sulfate (Na_2SO_4) + 25% Sodium chloride (NaCl) (wt % ratio). The hot corrosion behavior can be clarified by examining the corrosion kinetics, phase composition, and changes in the corrosion products of the alloy.

The influence of surface environmental damage on the tensile properties during the early stages of corrosion was studied. The purpose was to provide more guidance for understanding the corrosion–oxidation process of superalloys and evaluate strength degradation during service.

2. Materials and Methods

The experimental alloy was subjected to a triple process of vacuum induction melting (VIM), electro-slag remelting (ESR), and vacuum arc remelting (VAR). Then, the ingot was prepared for the homogenizing and forging process. The forging organization of 1130 °C solid solution treatment uses 850 °C and 760 °C double-stage aging to obtain the final heat treatment state specimen organization. The main chemical composition of the alloy is shown in Table 1 by ICP-AES.

Table 1. Main chemical composition in experimental alloy (wt %).

C	Cr	W	Mo	Ti	Nb	Al	Co	V	Ni
0.05	11.3	3.0	4.5	2.6	3.1	3.8	14.7	0.6	Balanced

The specimens (20 × 10 × 2 mm) were ground and polished according to HB5258-2000 [22]. Calcine the crucible until the change in mass is less than 0.0002 g. A 75% Na_2SO_4 + 25% NaCl (wt % ratio) salt mixture was placed in a crucible, keeping the molten salt just above the surface of the specimen for the hot corrosion test. Hot corrosion experiments were carried out in a muffle furnace in the air at 700, 750, and 800 °C for different times of 5, 10, 20, and 50 h. Under high-temperature salt bath conditions, the damage mechanism of new nickel-based superalloys in extremely harsh service environments was explored to initially explore the hot corrosion behavior and provide essential data for the next step of the long-term hot corrosion experiments.

The kinetic behavior in hot corrosion can be represented by the corrosion kinetic equation:

$$(\Delta W)n = kp \cdot t \quad (1)$$

The weight change per unit area at the experimental temperature, the rate exponent, the corrosion rate constant, and the experimental time are represented by ΔW, n, kp, and

t, respectively. After logarithmic treatment of both ends of the equation, the correlation corrosion rate constant can be found as follows:

$$Ln\Delta W = 1/nlnKp + 1/nlnt \quad (2)$$

After being immediately removed from the molten salts, the specimens were ultrasonically cleaned and rinsed with hot water to remove any remaining surface salt adhesions. Their mass changes were measured using an electronic balance that could weigh each specimen to within 0.0001 g. Three parallel specimens were put up for each hot corrosion condition to reduce experimental mistakes. Following the weighing process, the phase compositions of the corroded specimens were examined using an X-ray diffractometer operating at a scanning speed of 4° min^{-1} throughout the 10–100° range. Using Image-Pro Plus 6.0, a statistical analysis of the corrosion-related damage thickness of the scale was conducted. The Oxide Generation Gibbs Free Energy Change was calculated by HSC Sim 6.0 software. The thermophysical parameters required for simulation were calculated by JmatPro 7.0. The hardness of the sulfide scale was measured by nanoindentation device agilentG200 from KLA made in Milpitas, CA, USA. Scanning electron microscopy (JSM-7200F from JEOL Ltd. made in Tokyo, Japan) was used to characterize the surface and cross-section morphology of the hot corroded specimens. Energy-dispersive X-ray spectroscopy (EDS in JSM7200F) and an Electron Probe X-ray Micro-Analyzer (JXA-8530A from JEOL Ltd. made in Tokyo, Japan) were used to determine the elemental distribution of the oxidized specimens. Comparison of hardness of the environmental scale and substrate was obtained by the nanoindentation technique. GB/T228.1-2021 [23] requirements were utilized for the room-temperature tensile testing and mechanical characteristics of the corrosion specimen, with a dimension of M12 × φ5.

3. Results

3.1. Microstructure

The initial γ grains and γ′ precipitation phase microstructure are presented in Figure 1, and GB/T6394-2017 [24] estimates that the average grain size of the γ grains is approximately 24.65 μm. The nanometer-sized, almost spherical secondary γ′ phase particles coexist with the micrometer-sized irregular primary γ′ phase particles.

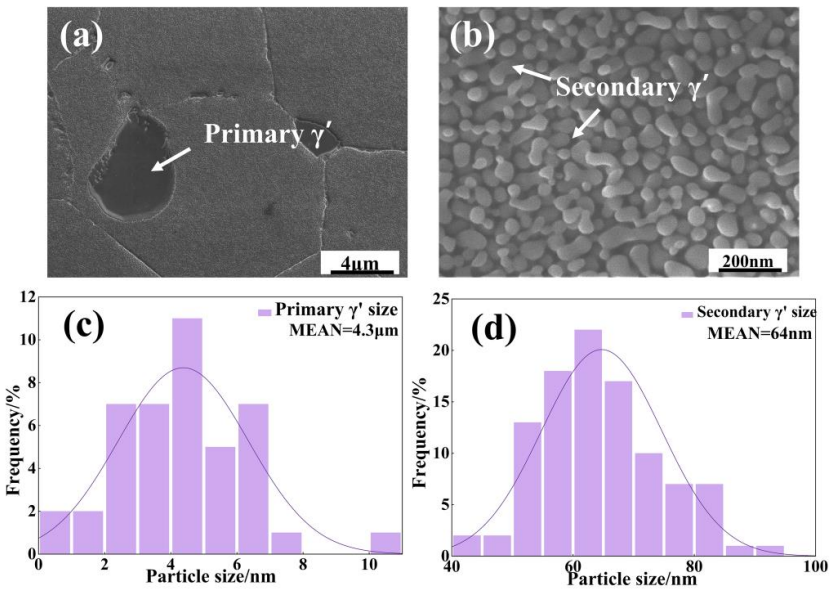

Figure 1. Characterization of the γ′ precipitation phase in the initial microstructure. (**a**,**b**) Microstructures; (**c**,**d**) average particle size of γ′ precipitation phase.

In addition, the primary γ′ phases of the micrometer scale can be seen at both grain boundaries and grains. The near-spherical secondary γ′ phases of the nanometer scale can be observed in the vicinity of the primary γ′ phases, which are statistically derived to be 4.3 μm and 64 nm in average size (the standard deviation is 1.97 and 9.93) for each level of precipitated phases, respectively.

3.2. Corrosion Kinetics

The relationship between mass variation and parameters is presented in Figure 2. The weight change of the experimental alloy is approximately 0.12441, 10.53473, and 160.10502 mg·cm^{-2} after 50 h of hot corrosion at 700, 750, and 800 °C. As 800 °C is close to the limit of the turbine disk alloy for the long-term service temperature, in the long-term salt bath conditions of the alloy, there is an inevitable surface thick corrosion layer shedding phenomenon. With the increase in corrosion time, the same experimental conditions of the weight of the individual workpieces under the weight change are relatively large. Figure 2b illustrates the link between the corrosion–oxidation parameters and mass change. The mass change rate of the experimental alloys increases with the increasing temperature.

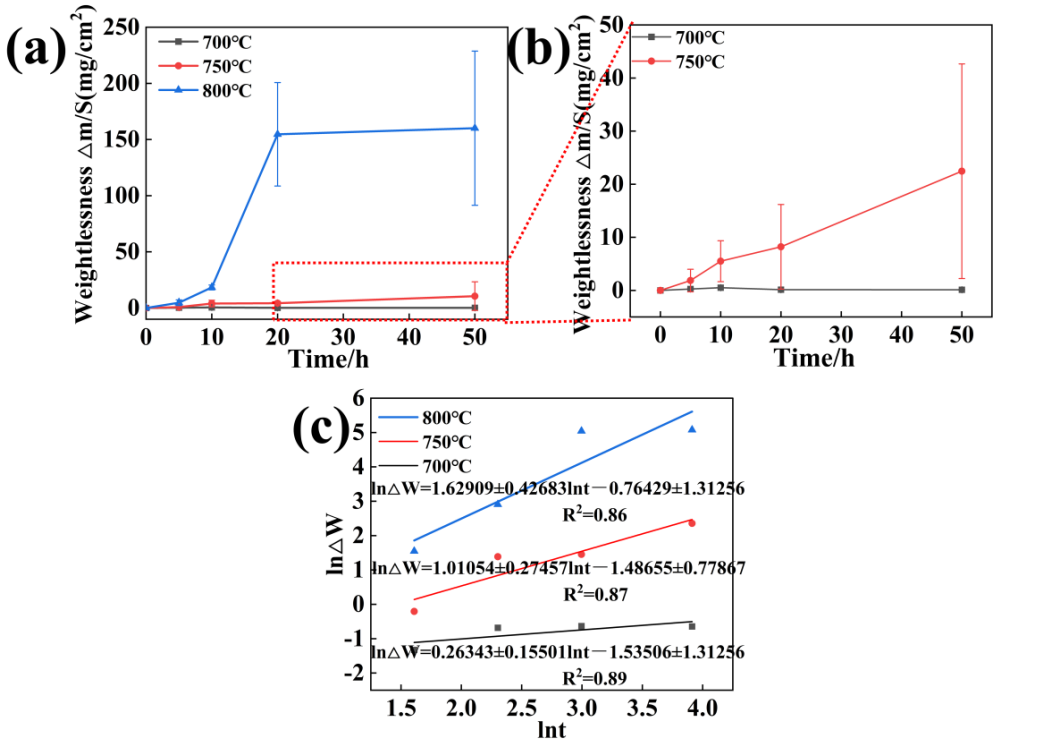

Figure 2. Relationship between mass variation and corrosion–oxidation parameters (**a**,**b**). Correlation between ln ΔW and lnt during hot corrosion. (**c**) Corrosion kinetic curves.

As seen in Figure 2a, the corrosion rate exponents at the experimental temperatures—800 °C: 0.625536, 750 °C: 0.229685, and 700 °C: 0.002946—are derived by calculating the slope and intercept of the straight line by the data points in the fitted graph. As shown in Figure 2b, the alloy corrodes much more quickly at 800 °C than it does with molten salt at 700 and 750 °C. When combined with the corrosion weightlessness kinetic curve, the corrosion kinetic curve exhibits a linear law in the early stages of corrosion. In the late stages, however, the corrosion is greatly increased due to oxidation, which causes the corrosion kinetic curve to change to a parabolic mode. This is not due to the formation of a protective oxide scale on the alloy surface but is instead due to corrosion leading to the partial cracking and spalling of the damaged scales, and these things enhance the corrosion rate and promote the failure of the superalloy [25,26].

3.3. Phase Composition of Corrosion–Oxidation Products During Hot Corrosion

Figure 3 shows the phases that constitute the damage scales after corrosion. The environmental damage mode of the alloy is dominated by oxidation and sulfides under the hot corrosion condition of a molten salt environment at 700–800 °C. The principal products of corrosion are oxides of Cr, Ni, Ti, and Al, as well as sulfides of Ni and Molybdenum (Mo). The structure of the hot corrosion process is comparatively complex, starting with a reaction based on Cr, Ni, Al, and a small amount of the spinel structure of the oxide and Mo sulfide at 700 °C. Until the late stage of the process started showing signs of Ti oxides and Ni sulfides, the spinel structures (nickel (II) chromate) of the peaks gradually increased. Under the conditions of 750 and 800 °C, with the increase in the experimental time, the oxidation and sulfide product change trend was roughly similar to 700 °C; it is worth noting that due to the rise in temperature, the surface protective layer in the early stage of the experiment appeared with Ni_3S_2. This demonstrates that hot corrosion is a synergistic process of oxidation and sulfidation [27]. In particular, the type of corrosion products analyzed by the XRD physical phase analysis of corrosion products under hot corrosion conditions is less at the late stage of corrosion, and the corrosion weight change curve is in line with this outcome.

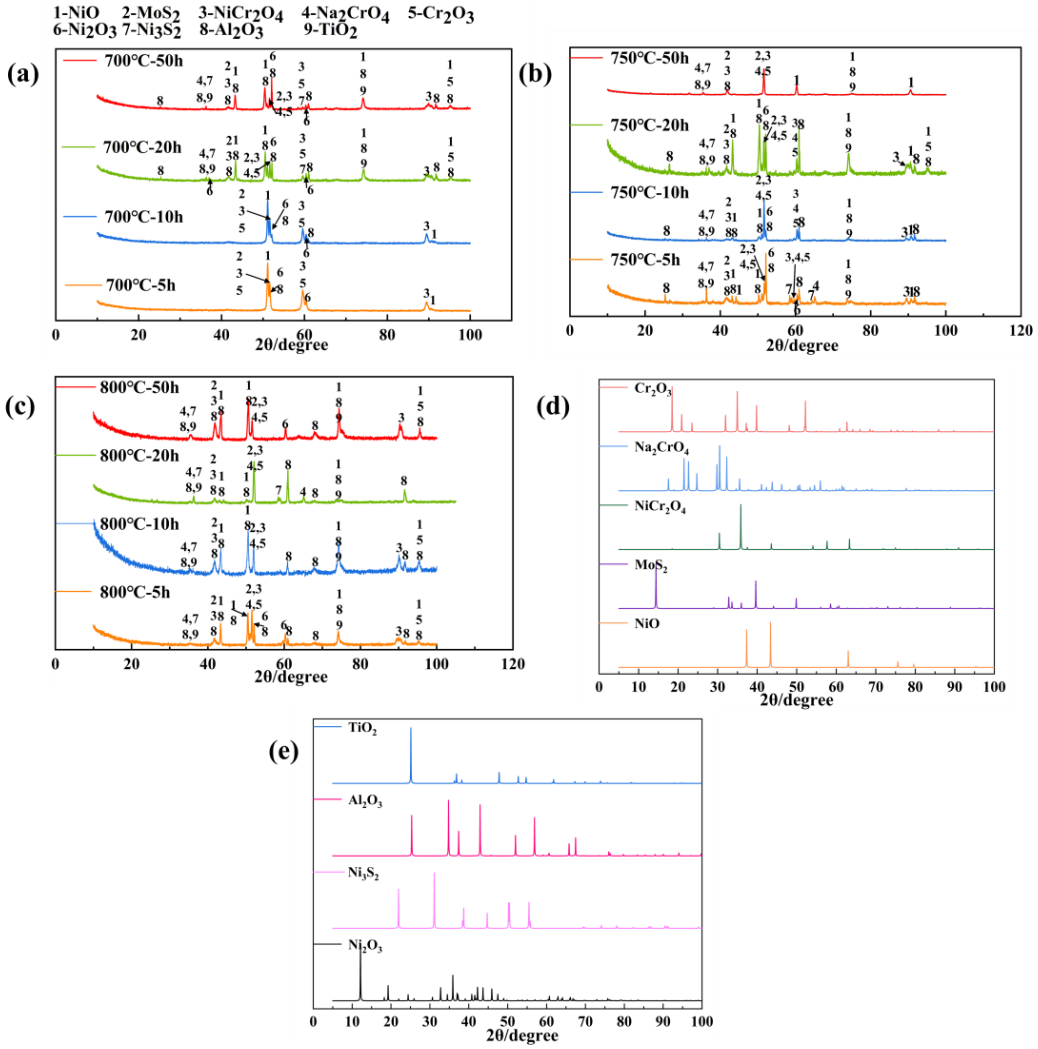

Figure 3. XRD pattern of hot corroded specimen at 700–800 °C. (**a**) 700 °C, (**b**) 750 °C, (**c**) 800 °C, and (**d**) and (**e**) represent theoretically simulated patterns based on the deposited crystallographic information files (cifs).

3.4. Corrosion Cross-Section Morphologies

The cross-section morphology and element distribution images of the specimens under corrosion are shown in Figures 4–6. The oxide scale, sulfide scale, and matrix organization are the three separate sections that make up the cross-section. In combination with the XRD results, this oxide scale is primarily in the form of Cr_2O_3 and Al_2O_3, whose presence can be used as a protective oxide to slow down the oxidation rate [28,29]. The Ni element also progressively diffuses to the surface, generating nickel (II) oxide (NiO) and Ni_3S_2 inclusions in the Cr_2O_3 oxide scale as the reaction time increases. In the inner scale of the corrosion product, the S and Mo elements are primarily mixed to create Molybdenum disulfide (MoS_2). As is shown in Figures 5 and 6, the Al elements exhibit a more positive response. This means that, at a higher temperature, the protection of the outer oxidation product is worse. The damage caused by the corrosion time extension to 50 h is severe: the thickness of the alloy matrix decreases significantly due to the gradual diffusion of the alloying elements Ni, Cr, Al, and Ti to form a thicker oxide scale. The Mo elements are found in the inner surface scale and throughout the damage scale.

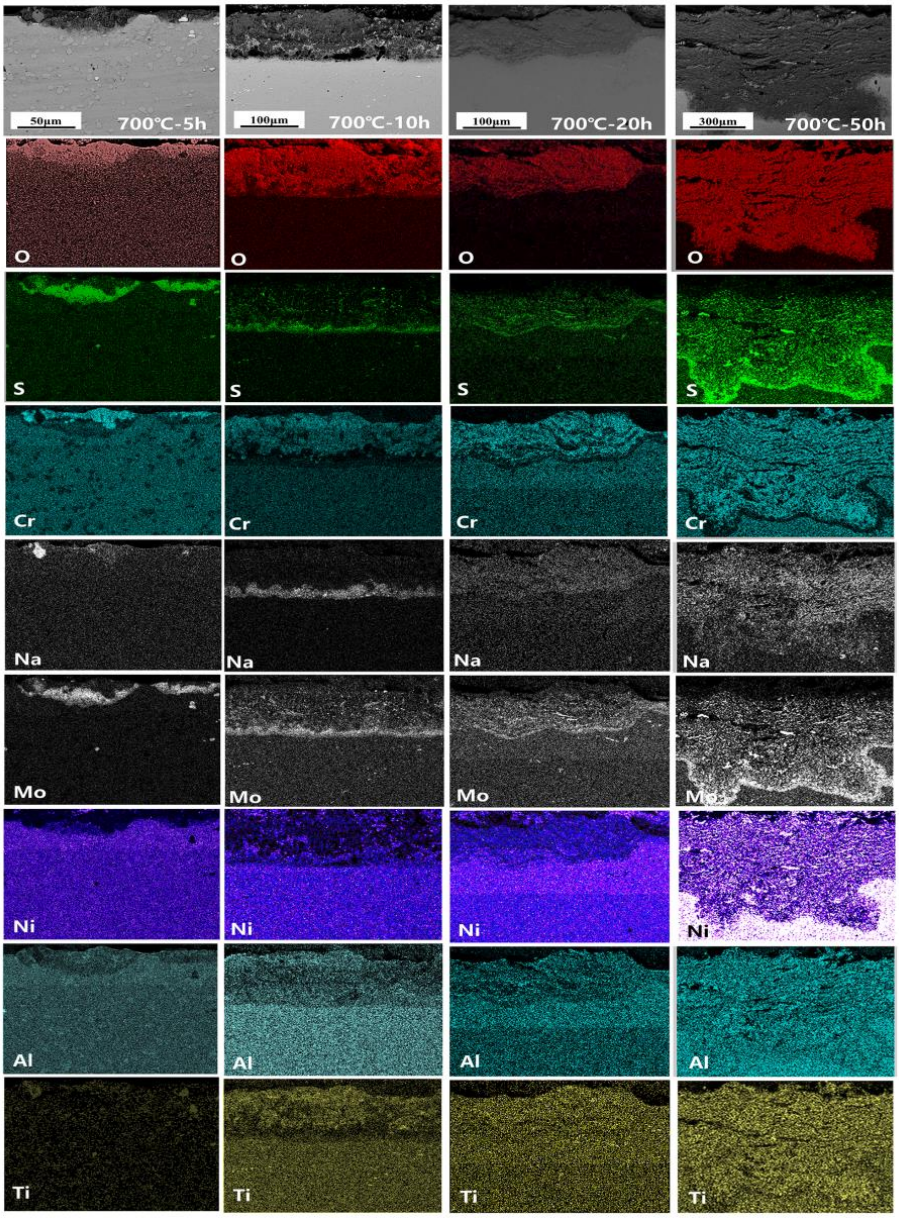

Figure 4. Cross-sectional morphology and elemental distribution of alloy at 700 °C.

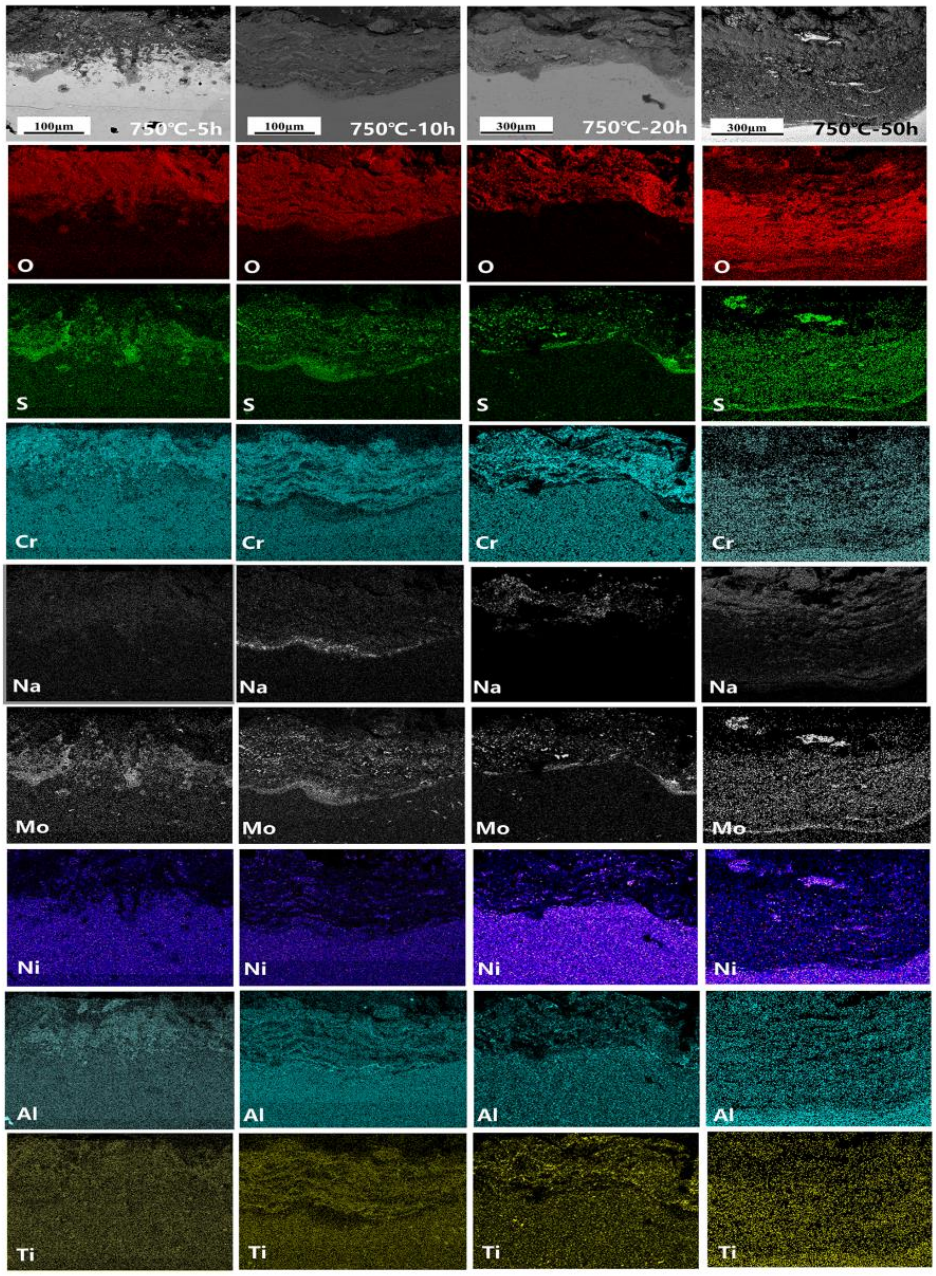

Figure 5. Cross-sectional morphology and elemental distribution of alloy at 750 °C.

The cross-sectional morphology of the early stage of corrosion is shown in Figure 7. The cross-section morphologies of the damage scales are affected differently by different temperatures. For example, the oxide and sulfide scales exhibit a clear delamination structure but no visible cracks or voids at 700 °C-5 h. At 750 °C-5 h, there are visible crack distributions in the oxide scales. Cracks and a few voids appear in the cross-section morphologies of damage scales at 800 °C-5 h. As the temperature increases, the sulfide scale becomes gradually thickened. This allows the metal to react with low-melting-point sulfides such as Ni_3S_2. It has a lower melting point and more crystal flaws with co-crystals, which enables the elements to diffuse quickly and creates a weaker scale that is more prone to damage [30,31]. Therefore, when the initial temperature increases, the corrosion of the oxide scale density gradually decreases until 800 °C when there are cracks and voids.

3.5. Comparison of Changes in Tensile Properties Before and After Hot Corrosion

The morphological observation and composition analysis of the corrosion products on the surface is shown in Figure 8. At 700 °C, the surface comprises a spalling defect, an oxide scale, and minor bumps. As the temperature rises, the bumps progressively get bigger, unite at 750 °C, and show many cracks at 800 °C. Because of oxidation and matrix element depletion, cracks may originate from the oxidized surface and grow quickly at high temperatures in service [32], hence decreasing the overall strength and causing premature failure. Figure 8 reveals some spalling of the oxide scale and that the Cr and Oxygen (O) elements predominate in the oxide protective scale. Bump defects are mainly composed of Ni and Cr oxides, and as the temperature increases here, the Cr contrast is relatively reduced. As shown in Table 2, the Ni element ratio is significantly higher in bump defects than in surface oxide scale structure. Because the "oxidation-sulfidation" mode of the hot corrosion reaction allows corrosive elements to pass through the oxidation scale to alloy, as a result, the Cr_2O_3-based oxide scale is inevitably be destroyed, resulting in a small number of defects in the composite oxide scale.

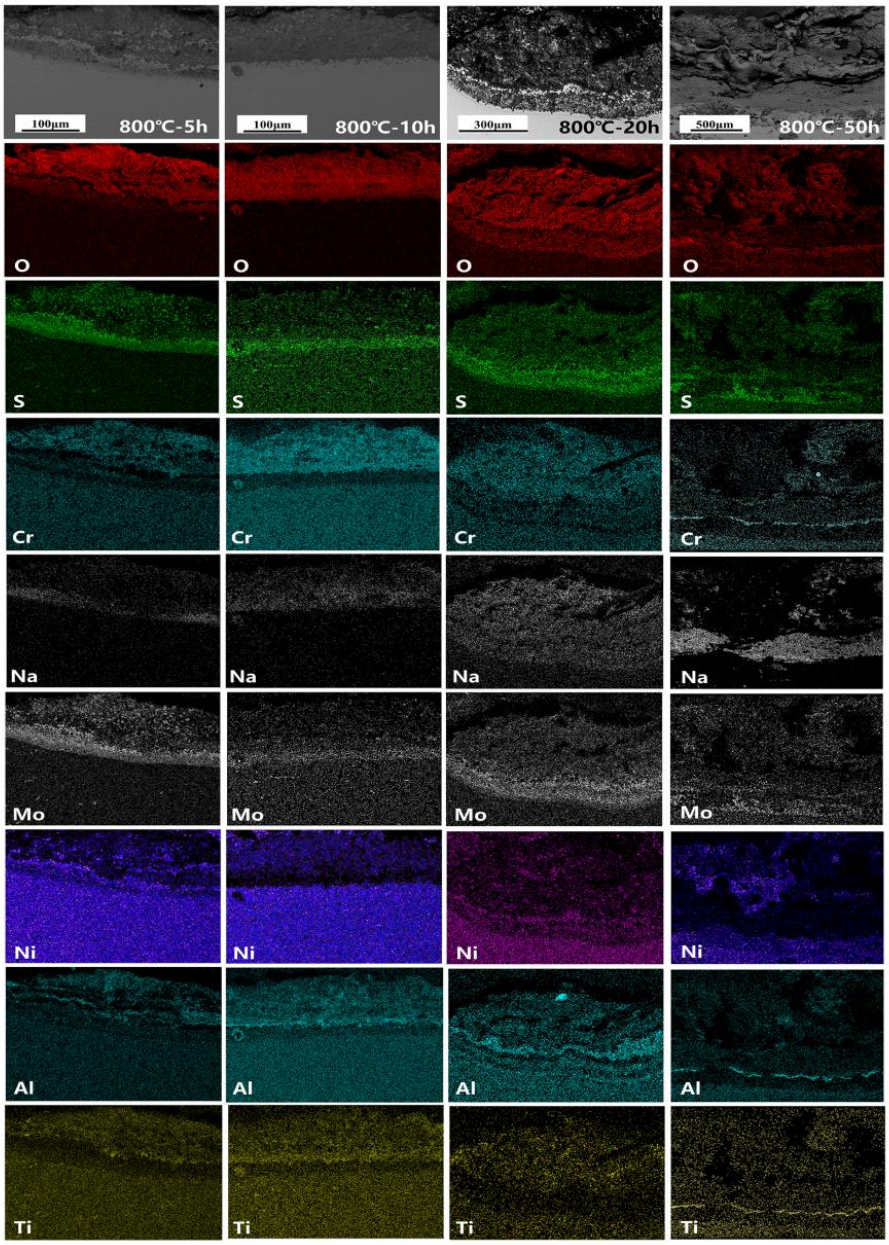

Figure 6. Cross-sectional morphology and elemental distribution of alloy at 800 °C.

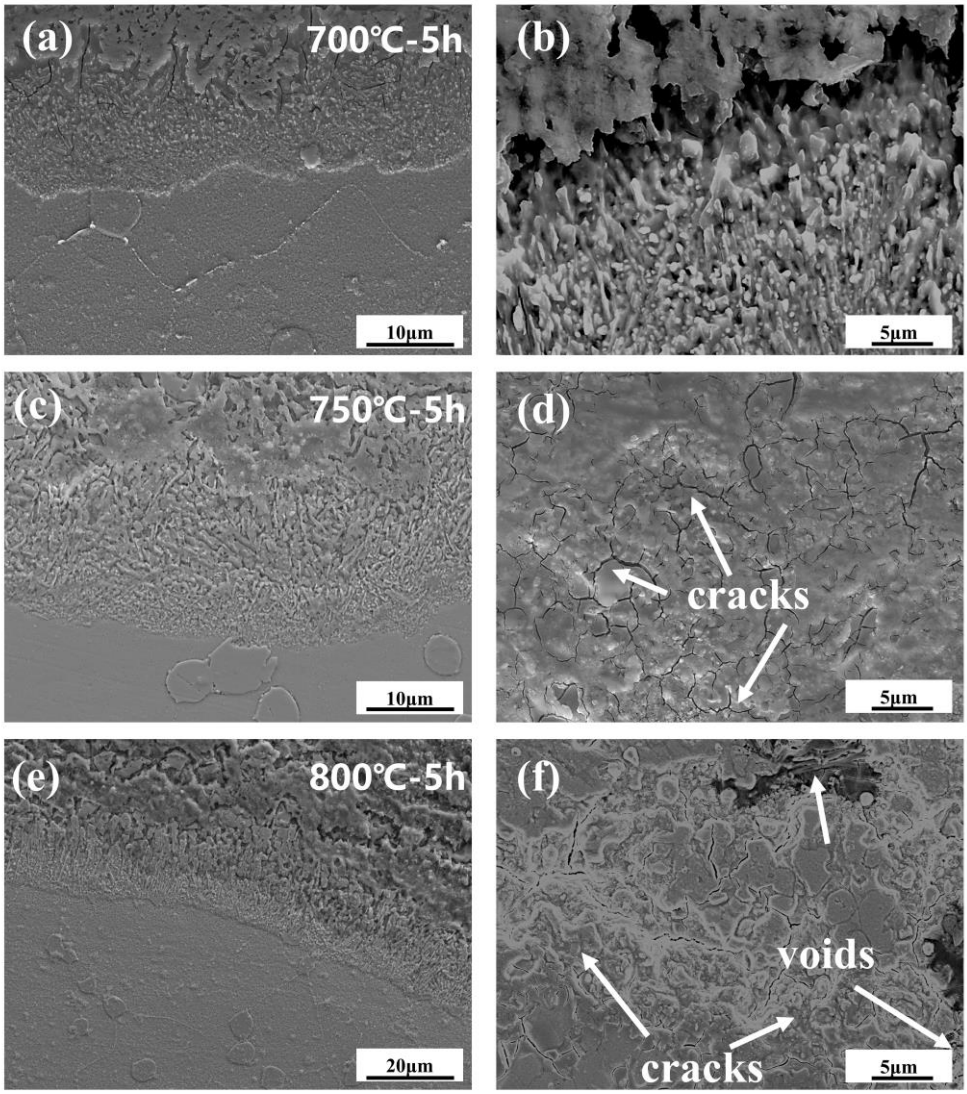

Figure 7. Cross-sectional morphology of the oxidized sulfide matrix at the early stage of corrosion at 700–800 °C. (**a**,**b**) 700 °C-5 h, (**c**,**d**) 750 °C-5 h, (**e**,**f**) 800 °C-5 h.

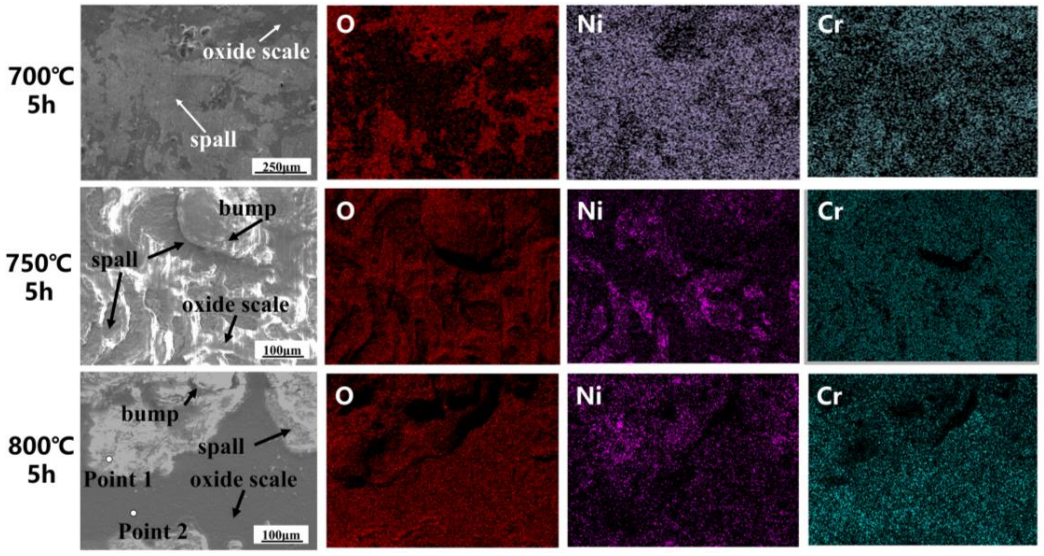

Figure 8. Analysis of the main components of the corroded surfaces at 700, 750, and 800 °C-5 h.

Table 2. EDS compositional analysis elemental content.

	O	Al	S	Ti	Cr	Ni
Point 1	37.69	1.81	0.49	2.55	15.22	42.24
Point 2	48.98	1.93	2.91	7.64	32.37	6.76

The distribution of element components in the damaged scale is illustrated in Figures 9–11. A more detailed view of a small amount of the Al_2O_3 subscale between Cr_2O_3 and MoS_2 at 700 °C and 750 °C is also visible. Unlike in the studies by Yu et al. [33] and Han et al. [34], the alloy does not have a significant depleted scale of Cr present in the matrix organization after hot corrosion; in the present experiments, it is mainly replaced by MoS_2. The Ni elements are also visible in the aggregation of the inner surface scale and in a small portion of the diffusion phenomenon to the surface. Notably, the Ni elements exhibit a significant outward diffusion at 800 °C-5 h, increasing the percentage of Ni sulfides and oxides in the damage scale. In contrast, the Ti elements show a positive oxidative response by progressively diffusing into the outer surface scale. This indicates that the Cr_2O_3-based oxide scale provides some protection during the early stages of hot corrosion, but the protective effect is gradually reduced with temperature with extensions.

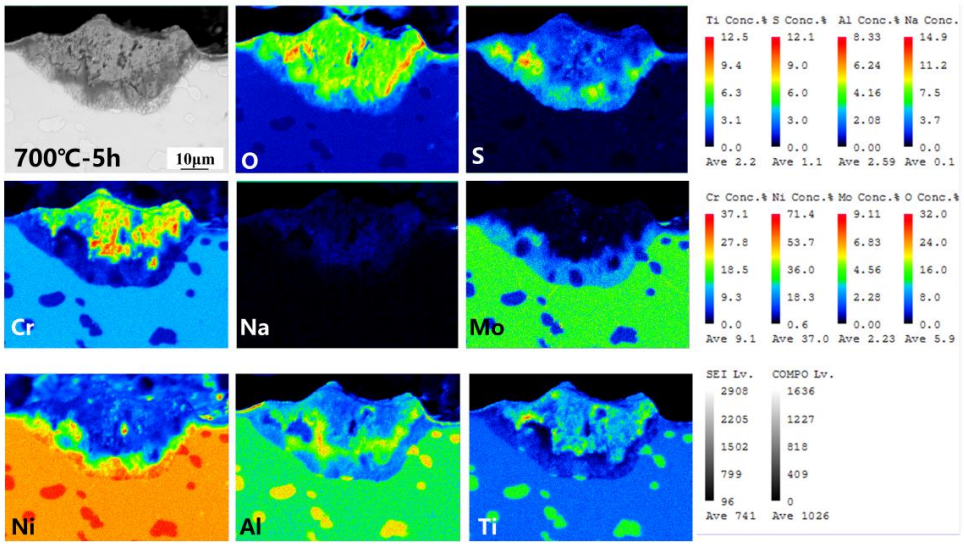

Figure 9. Element distribution of experimental alloy after hot corrosion at 700 °C-5 h.

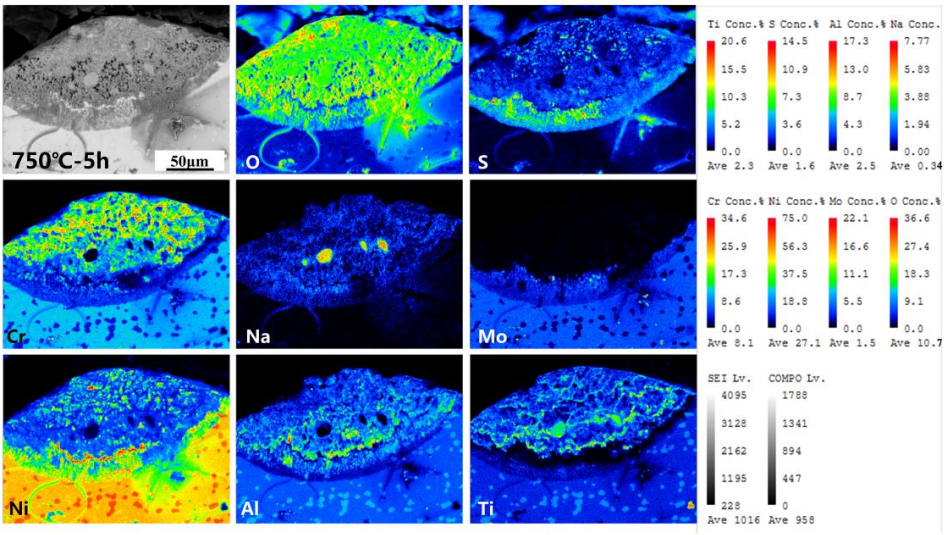

Figure 10. Element distribution of experimental alloy after hot corrosion at 750 °C-5 h.

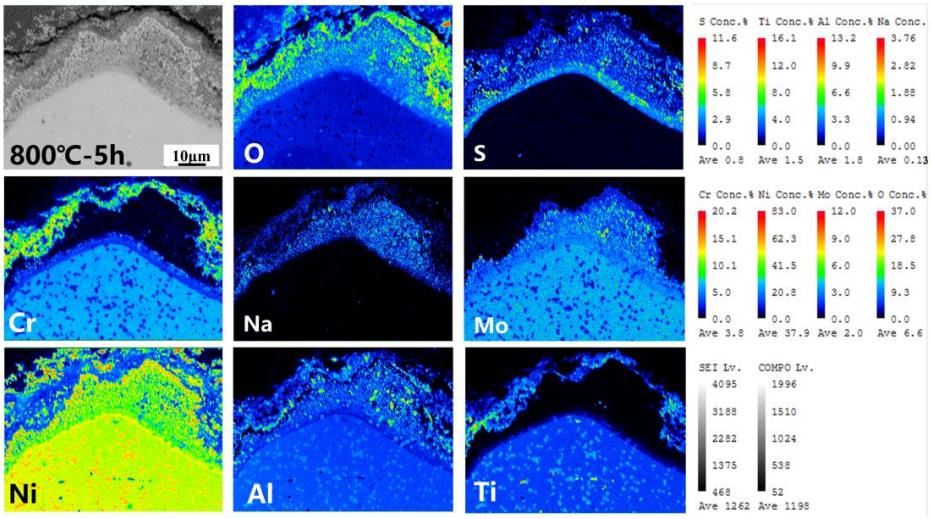

Figure 11. Element distribution of experimental alloy after hot corrosion at 800 °C-5 h.

As can be seen in Figure 12, the yield strengths exhibit a declining trend during hot corrosion. The tensile yield strength of the alloy decreases by 3.3, 3.8, and 6.1% at 700, 750, and 800 °C, respectively, from the standard heat-treated state specimens. A total of 800 °C has a greater effect on the strength properties of the alloy. This trend is mainly associated with microstructures and the element consumption of specimens. This indicates that the extent of sulfide damage to the protective layer increases as the thermal corrosion temperature increases, which is consistent with the EPMA results above. Although just three temperature point specimens were used to assess the mechanical properties of the corroded alloys, the trend of how the damaged structure affected the strength characteristics was identifiable.

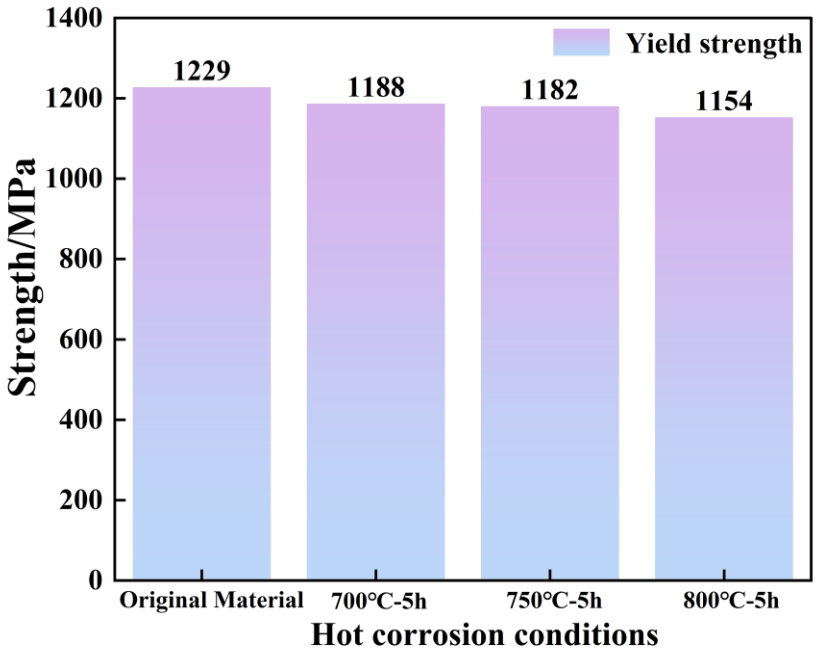

Figure 12. Trends in room-temperature yield strength properties under various conditions.

4. Discussion

4.1. Corrosion–Oxidation Mechanism

The corrosion–oxidation mechanism can be summed up based on the discussion above. The oxide generation free energy change calculated by HSC Sim in 600–800 °C is illustrated

in Figure 13. It has been demonstrated that the element Cr of binary alloys (such as Ni-Cr) significantly affects the oxidation rate constants of alloys. The oxidation rate constants Kp for Al_2O_3 and Cr_2O_3 are several orders lower than for NiO and CoO. As a result, it is easier to form a protective Al_2O_3 or Cr_2O_3 scale on the alloy surface [35]. The most active elements react with oxygen to form oxides that grow inward from the surface of the alloy, which is called internal oxidation [36]. The Al element shows the most significant driving force due to the lowest formation energy, which preferentially promotes the growth trend of Al_2O_3. However, the diffusion rate of Cr is much higher than that of Al; Cr_2O_3 grows at a higher rate than the Al_2O_3 oxide scale, so the early stage of oxidation preferentially forms Cr_2O_3, and Al_2O_3 exists in the form of internal oxidation. At the same time, the Cr element in superalloys primarily resides as a Cr_2O_3 outer surface oxide because it is more active than NiO, causing the replacement reaction [37].

$$3NiO + 2Cr \rightarrow 3Ni + Cr_2O_3 \quad (3)$$

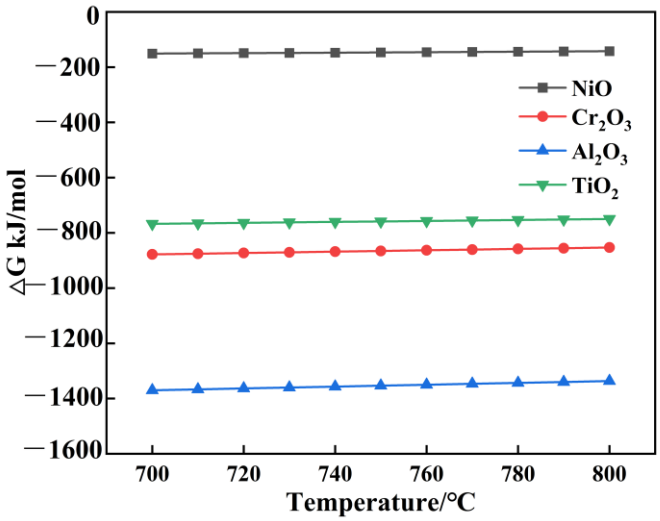

Figure 13. Total of 600–800 °C Oxide Generation Gibbs Free Energy Change.

With the deepening corrosion conditions, the Cr_2O_3 scale becomes loose and even cracks; at this time, the Ni element as a matrix element quickly diffuses to the surface, furthering the bump enrichment and gradual thickening. Secondly, a tiny amount of TiO_2 and Al_2O_3 is formed on the surface as the Ti and Al elements progressively diffuse outward. Furthermore, the produced spinel-structured oxides, such as nickel (II) chromite ($NiCr_2O_4$), might further deteriorate the surface densification and increase the degree of corrosion [15].

$$NiO + Cr_2O_3 \rightarrow NiCr_2O_4 \quad (4)$$

In addition to the oxidation mechanism, however, the role of the corrosive medium should not be ignored. According to pertinent research, while corrosion occurs in an environment with 75% Na_2SO_4 + 25% NaCl molten salt, the molten NaCl dissolves the protective Cr_2O_3 scale by penetrating the oxide scale and reacting directly with Cr_2O_3. On the other hand, the competition of dissolution and forming finally results in a loose oxide scale when the molten salt combines with oxides like Cr_2O_3 [38–40]. The reaction equations are as follows:

$$4NaCl + O_2 \rightarrow 2Cl_2 + 2Na_2O \quad (5)$$

$$Na_2SO_4 \rightarrow SO_3 + Na_2O \quad (6)$$

$$Na_2SO_4 \rightarrow Na_2O_2 + SO_2 \quad (7)$$

$$Cr_2O_3 + 3Na_2O_2 \rightarrow 2Na_2CrO_4 + Na_2O \quad (8)$$

$$2Cr_2O_3 + 3O_2 + 4Na_2O \rightarrow 4Na_2CrO_4 \quad (9)$$

$$4NaCl + Cr_2O_3 + 5/2O_2 \rightarrow 2Na_2CrO_4 + 2Cl_2 \quad (10)$$

So, the primary factor in the deepening of corrosion–oxidation damage in high temperatures is the lapse of protective oxides, whereby the migration of Ni and Cr elements to the surface is the primary cause of the oxide scale thickening. The oxidation response of the Al and Ti elements is observed to be more positive at higher temperatures and longer corrosion times. This phenomenon is also one of the factors responsible for the thickening of the corrosion oxidation product scale. Additionally, the depletion of alloy elements, such as Ti and Al, could promote crack initiation, ultimately leading to the mechanical property degradation of the alloy. In summary, the corrosion and oxidation mechanism diagram is shown in Figure 14.

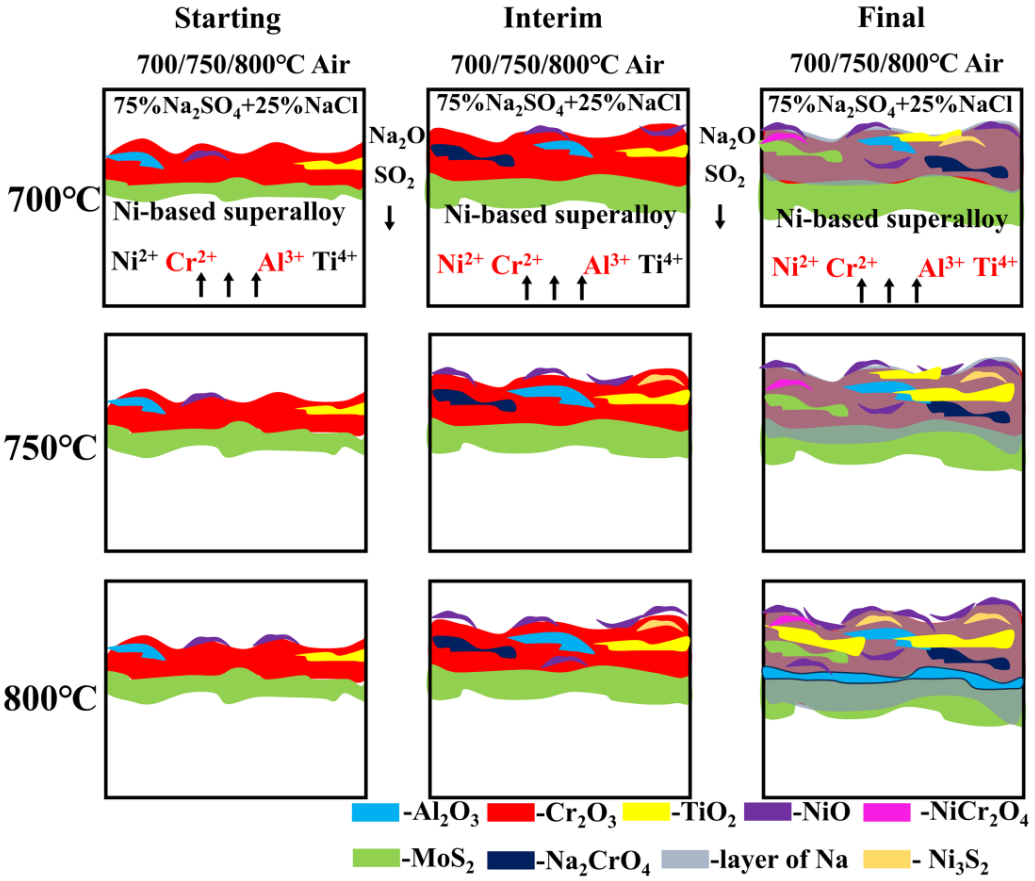

Figure 14. Corrosion–oxidation process schematic diagram.

The percentage of the sulfide scale exhibits a growing trend with increasing temperature (700 °C-50 h: 30 μm, 750 °C-50 h: 33 μm, and 800 °C-50 h: 208 μm). The formation of the sub-surface scale of the more dense Al_2O_3 also has a specific reduction in the diffusion of matrix components to the exterior at the hot corrosion temperature of 800 °C. However, the outer Cr_2O_3 oxide scale repeatedly undergoes a "dissolution-regeneration" process, which results in the penetration of the S elements into the oxide scale and the matrix. This leads to the deeper penetration of sulfide damage, and a complicated oxidation–sulfidation damage structure is produced. The following is the reaction equation: sulfur damage predominates in this molten salt environment at temperatures of 800 °C, whereas oxida-

tion damage predominates at temperatures of 700 °C and 750 °C, with sulfide damage as a supplement.

$$3Ni + 2S \rightarrow Ni_3S_2 \quad (11)$$

$$4Na_2SO_4 + 18Ni + 2Cr_2O_3 + 3O_2 \rightarrow 4Na_2CrO_4 + 12NiO + 2Ni_3S_2 \quad (12)$$

4.2. Formation of Crack and Spalling

Spalling can potentially come from oxide internal stresses. One type of growth stress is caused by the growth and formation of the oxide. The other is thermal stress generated from different coefficients of thermal expansion (CTEs) in the metal/oxide system [15,41]. The volume difference of oxides and metal is the primary source of growth stresses. The volume difference at the scale/alloy contact where the oxide forms can be represented by the Pilling–Bedworth ratio (PBR):

$$PBR = \frac{v_{oxides}}{v_{alloy}} \quad (13)$$

$$\varepsilon = \sqrt[3]{PBR} - 1 \quad (14)$$

$$\sigma_G = \varepsilon Eoxides \quad (15)$$

Table 3 displays the relevant parameters and calculations. V_{oxides} and V_{alloy} are the oxide and metal volumes, respectively, and E_{oxides}, ε, and σ_G stand for the oxide Young's modulus, growth strain, and stress.

Table 3. PBR, E_{oxide}, and σ_G of oxides in oxide scale [13].

Oxides	Cr_2O_3	$NiCr_2O_4$
PBR	2.07	2.05
E_{oxides}	260	233
σ_G	71.35 GPa	62.99/GPa

In the cooling process, thermal stresses arise. The different thermal expansions in the oxide scale and the alloy cause thermal stresses. Consequently, the following formula can be used to determine the thermal stress or σ_T:

$$\sigma_T = Eoxides\left(\alpha_{alloy} - \alpha_{oxides}\right)\Delta T \quad (16)$$

where ΔT is the difference in temperature during cooling, and α_{alloy} and α_{oxides} are the respective coefficients of the thermal expansion of oxides and metal. The computed temperatures were set to 700, 750, and 800 °C. The coefficients of thermal expansion of the alloys were determined by the software JmatPro7.0; α_{alloy} was found to be 1.52×10^{-6} K^{-1}. Table 4 displays the parameters and the results of the computation.

Table 4. α_{alloy} and α_{oxide} of oxides and alloy [13,42].

Oxides	Cr_2O_3	$NiCr_2O_4$
α_{oxides}	9.6×10^{-6} K^{-1}	7.6×10^{-6} K^{-1}
α_{alloy}	15.2×10^{-6} K^{-1}	15.2×10^{-6} K^{-1}
σ_T (700 °C)	0.99 GPa	1.20 GPa
σ_T (750 °C)	1.06 GPa	1.29 GPa
σ_T (800 °C)	1.13 GPa	1.38 GPa

From computations, thermal stresses are orders of magnitude smaller than the growth stresses. Research has revealed that [43,44] when PBR > 1, stress can be called compressive

stress in the oxide scale. On this basis, it can be concluded that the cracking and spalling of the oxide are caused by growth stresses and promoted by thermal stresses, which explains how oxides crack and spall.

In this study, the experimental alloy shows rapid corrosion rate constants because of its relatively low Cr and Al element content. The oxidation of the Cr and Ni elements accounts for a significant proportion. During the hot corrosion phase, the Ni element diffusion primarily occurs when the protective Cr_2O_3 is generated and dissolved. This leads to the O element invasion process, which quickly produces NiO and thickens the oxide scale quickly. Simultaneously, the S element intrusion reacts with the Mo and Ni elements in the matrix to form an inner scale MoS_2 sulfide scale and Ni_3S_2 inclusions. The alloy matrix corrodes rapidly due to the outward diffusion of Ni, Cr, and other elements, forming corrosion pits on the matrix surface. As temperatures approach 700–800 °C, contaminants such as salt from the intake air, engine components, and combustion may erode the protective oxides on these discs' surface. When the salt locally reduces these oxides, pits appear, and the protection is lost [45]. Unlike usual investigations, the larger thickness of the corrosion–oxidation scale prevented the appearance of pits on the surface. The research of Timothy [46] is similar to our findings, revealing that the oxide scale was occasionally kept in and on the pits. Figure 15 illustrates the pits in the early phases of corrosion at 700, 750, and 800 °C, covered by an oxide scale. With the temperature increase, the pit deepened. Research demonstrates that [47] at the bottom of the corrosion pit surface, localized corrosion is formed and grows along the grain boundaries. The sensitive grain boundaries cause very early fatigue crack initiation at 704 °C. Eventually, the pit becomes severely damaged due to the matrix microstructure.

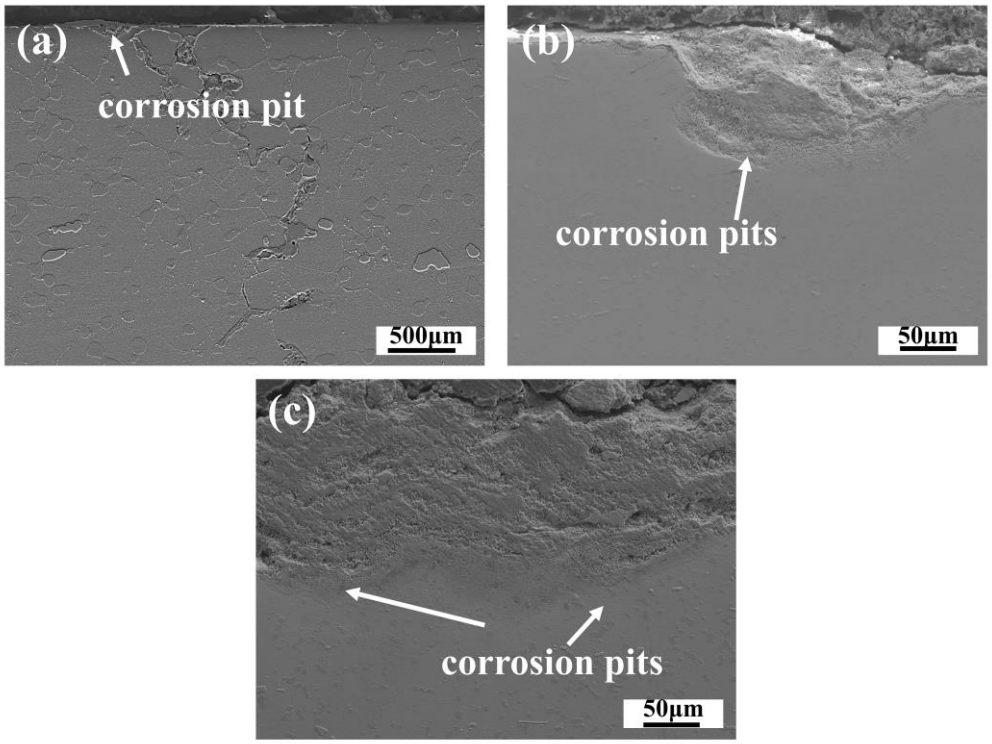

Figure 15. Corrosion pit morphology. (**a**) 700 °C-5 h, (**b**) 750 °C-5 h, (**c**) 800 °C-5 h.

4.3. Mechanism of Competition for the Element Diffusion

Currently, conventional heat-resistant alloys obtain oxidation resistance by the diffusion of Cr outward to form a dense Cr_2O_3 scale on the surface. But when exposed to high temperatures and pressures in a water vapor environment, Cr_2O_3 readily forms the unstable hydroxide chromium (IV) hydroxide (CrO_2 $(OH)_2$), which is unstable and volatilized.

This severely compromises the integrity of Cr_2O_3 and eliminates the protective function of the oxide scale. Many researchers focus on the Al_2O_3-type oxide scale, which has the same corundum structure, density, and strong bonding force as the matrix to tackle volatility at high temperatures. The Al_2O_3 type has a lower oxidation rate than that of the Cr_2O_3 type. This is primarily due to the slower growth rate, higher thermodynamic stability, and higher antioxidant capacity in the high-temperature water vapor environments of Al_2O_3. Additionally, in many service environments, the effect of oxidation protection is more prominent [48]. Ni-Cr-Al alloys can be classified into three categories based on their oxidation behavior: a non-protective external NiO scale with discontinuous Cr_2O_3 and Al_2O_3 intrusions is called a type I alloy; type II alloys combine a discontinuous Al_2O_3 intrusion phase suboxide scale with an external Cr_2O_3 continuous oxide scale; and type III alloys create an uninterrupted Al_2O_3 exterior oxide scale [49]. Combining the experiment results in this study, it is clear that the experimental alloy does not exhibit a precise continuous Al_2O_3 scale at 700–750 °C. The increase in temperature leads to the gradual appearance of the continuous internal oxide scale structure of Al_2O_3 at 800 °C. In a gas turbine engine, the current temperature of the turbine disk typically does not exceed 750 °C. If polycrystalline superalloys can form Al_2O_3 (type III) instead of Cr_2O_3, experimental alloys could benefit more fuel-efficient gas turbine engines in the future. Consequently, the computational approach [50] has been usually used to predict the tendency toward preferentially formed protective oxides. Wagner [51] assumed that the transition from internal to external oxide formation occurs if the solute concentration is high enough to cause the volume fraction of internal oxides to be more significant than a critical volume fraction. However, with regard to Al_2O_3, an external protective oxide scale appears to fail in the experiment. This requires the help of the formula for the lowest solute concentration needed in a binary A–B system to initiate external oxidation:

$$N_B^O = \left[f\left(\frac{V_m}{V_0 x}\right) \pi \frac{N_O^S}{2\nu} \frac{D_O}{D_B} \right]^{\frac{1}{2}} \tag{17}$$

$$N_0^S = 8.3 \cdot \exp\left[\frac{-55\frac{kJ}{mol}}{RT}\right] \tag{18}$$

$$D_O = 1.7 \times 10^{-5} \cdot \exp\left[\frac{-90\frac{kJ}{mol}}{RT}\right] \tag{19}$$

$$D_B = 1.1 \cdot \exp\left[\frac{-249\frac{kJ}{mol}}{RT}\right] \tag{20}$$

where N_B^O represents the minimum critical concentration of solute B required for external oxidation, and V_m denotes the molar volume of the alloy at a specific temperature ($cm^3 \cdot mol^{-1}$). This portion is determined to be 7.20 ($cm^3 \cdot mol^{-1}$) at 800 °C calculated by Jmatpro 7.0. The molar volume of Al_2O_3 (V_{ox}), which stands for the molar volume of oxides ($cm^3 \cdot mol^{-1}$), is computed using the standard density and molecular weight values from Refs. [26,52], and its value is 25.575 $cm^3 \cdot mol^{-1}$. N_O^S is the solubility of oxygen in the alloy, expressed as a mole fraction; Equation (18) illustrates the O element in the Ni-based component of the solubility; D_O denotes the diffusion rate of Ni in the alloy, and it can be roughly calculated using the diffusion rate of O in the Ni matrix, as indicated by Equation (19) [53]. According to Equation (20), D_B is the solute diffusion rate of Al in the Ni matrix (in $cm^2 \cdot s^{-1}$) [54]. The value of v can be defined as the ratio of element O stoichiometry to element B, which is, for example, 1.5 in the case of Al_2O_3. It is pretty

realistic to use 0.3 as the volume fraction f of the internal oxides based on the research of Nesperson [55] and Pettit [56]. Table 5 displays the computation and simulation results.

Table 5. Parameter values for the lowest critical Al content needed to cause the alloy to externally oxidize at 800 °C.

V_m	N_0^s	D_O	D_B	N_B^O
7.20	1.75×10^{-4}	7.07×10^{-10}	8.34×10^{-10}	9.78%

Based on theoretical calculations, the Al_2O_3 oxide scale is generated as an external oxide scale when the alloy system contains 9.78% (wt %) of Al. Consequently, under 800 °C hot corrosion conditions, the continuous Al_2O_3 oxide scale forms only in the inner scale and thickens gradually over time. However, it is worth noting that oxygen filling decreases under hot corrosion conditions in molten salts, and the Al external concentration may increase.

4.4. Corrosive Properties Damage

The fracture morphology of RT tensile specimens under different corrosion conditions is shown in Figure 16. The fracture morphology is flat and microscopically characterized by intergranular brittle fractures in the presence of cleavage steps. These features include blocky steps, river patterns, and intergranular cracks. The elongation exhibits a declining trend when the cracks proliferate during the tensile process, even when the strength properties are not severely affected [15]. As shown in Figure 16c,d,g,h,k,l, the longitudinal section near the tensile fracture showed significant sulfide scale cracking. This cracking source extended to the matrix and affected the mechanical characteristics by causing intergranular cracks. Furthermore, more severe cracks in the matrix occur due to the rapid expansion along the phase boundary between the primary γ' and the matrix.

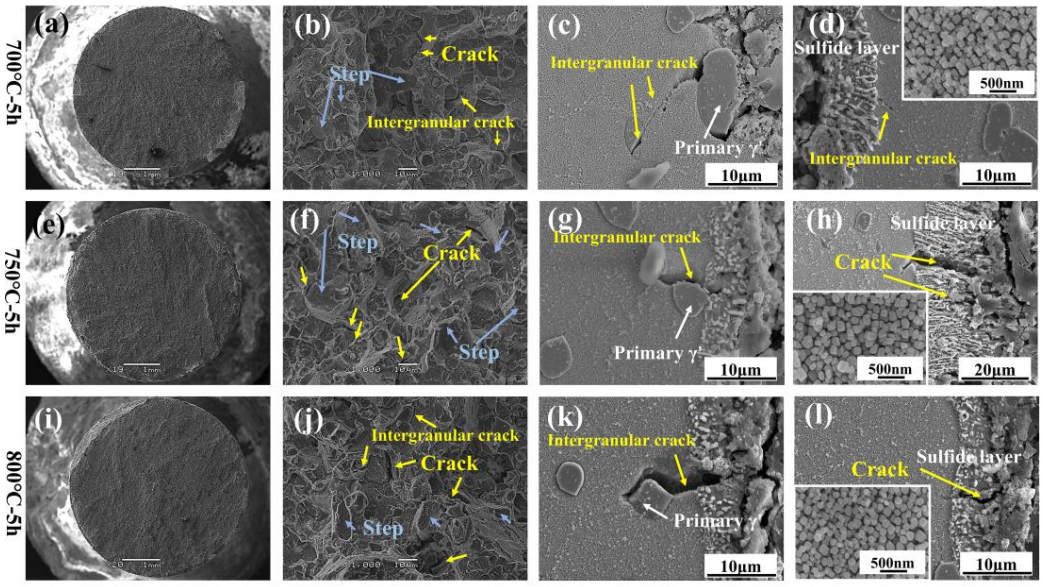

Figure 16. Fracture morphology of RT tensile specimens under different corrosion conditions. (**a**,**b**,**e**,**f**,**i**,**j**) fracture morphology, (**c**,**g**,**k**) cracks between primary γ' and matrix, (**d**,**h**,**l**) cracks in sulfide scale.

The hardness of the substrate and oxide–corrosion scale under various conditions were determined by the nanoindentation test method in Figure 17d. If the indentation depth is set at 100 nm, the hardness of the sulfide-damaged scale is significantly lower

than that of matrix. This suggests that there will be more plastic deformation in this area during the deformation process, leading to significant strain localization, which is the reason that causes the sulfide scale to crack. According to Figure 17a–c, the loss of properties is marginally less at 700 °C due to the much thinner damage scale than at 750 and 800 °C under 5 h conditions. Due to the thin thickness of the corrosion early damage scale at 700 and 750 °C, the thickness of the sulfide scale does not differ much, so the yield strength decline is slightly lower and more similar. When the thickness of the sulfide scale is more significant at 800 °C, the strength properties are of a more considerable degree of attenuation.

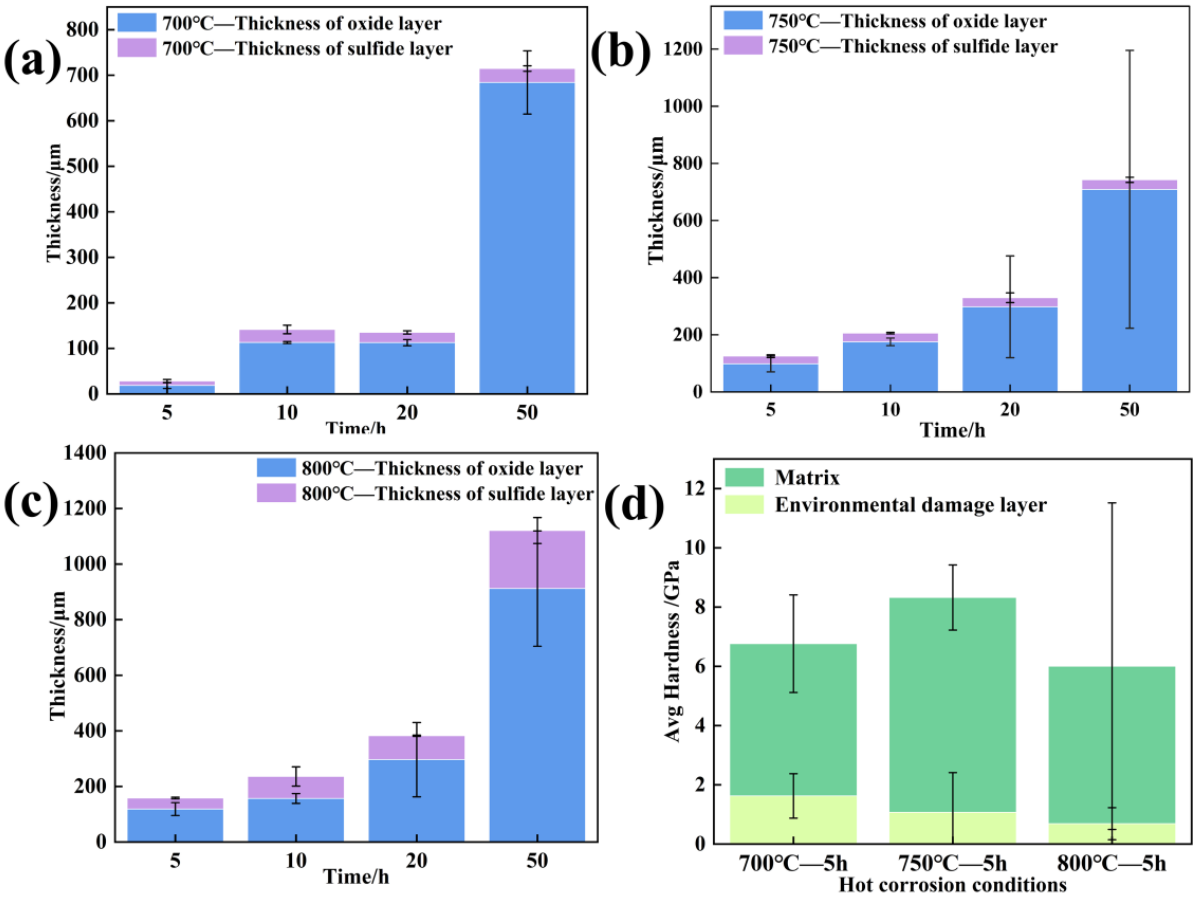

Figure 17. Characteristics of environmental damage scales and matrix under different hot corrosion conditions. (**a**–**c**) Thickness and (**d**) hardness.

The PBR value of the oxide scale is greater than one, so the compressive stress placed on the matrix theoretically can protect the material and increases the role of the force area. However, in extremely hot corrosion conditions, the oxide scale is substantially damaged, and the beneficial effects of the scale are not realized [57]. In addition, there are localized pits on the alloy surface because of inhomogeneous hot corrosion [58]. The force area then shrinks to create a localized stress concentration, which has an additional impact on the mechanical characteristics [46,47].

In the foundation of the corrosion–oxidation mechanism, the following impacts of the mechanical characteristics of the hot corrosion process are summarized: (1) since the spalling of the surface damage scale may accelerate the substrate corrosion, the stress concentration increases, and the effective bearing area of the specimen is reduced; (2) surface pits and bumps are created by the cracking and spalling of the hot corrosion scale, which concentrates stress and speeds up the formation of cracks; (3) under load, microcracks

propagate into the matrix through the sulfide scale, ultimately leading to fracture and significantly influencing properties; (4) strain localization and accelerated crack initiation may result from plastic deformation which is exacerbated by the decreased hardness of the sulfide scale.

5. Conclusions

This study systematically investigates the hot corrosion behavior of a new nickel-based high-temperature alloy under different conditions and its effect on the alloy properties. Analyzing the composition of corrosion products, the damage mechanisms, and the impact of corrosion on properties provides crucial theoretical support for applying the alloy in high-temperature environments. However, thermal corrosion is a complex multifactorial process, and future research can further improve the corrosion resistance of alloys by developing new protective coatings, optimizing alloy compositions, and simulating corrosive environments that are closer to actual working conditions. These research directions will not only help solve the current corrosion problems faced but also provide broader prospects for designing and applying superalloys. The main conclusions of this paper are as follows:

1. The damage scale is composed of inner sulfides and external oxides, and the hot corrosion element diffusion mechanism is governed by the diffusion of the Cr, Ni, Al, Ti, and Mo elements. At 700 °C and 750 °C, oxidized damage predominates, and at 800 °C, sulfurized damage takes center stage.
2. Since the crucial generation conditions of external oxides are not met, the Al element content appears as a sub-surface scale at 800 °C, with Cr_2O_3 making up the majority of the surface scale oxides.
3. During steady-state hot corrosion, the sharp increases in growth stress caused by the formation of oxides and spinels are the leading cause of the cracking and spalling of the composite oxide scale. With the increase in corrosion, there also exists a damage mechanism of dissolution–regeneration–dissolution in the surface oxide organization.
4. The main effects of hot corrosion on the alloy's tensile properties are the exfoliation cracking of the surface oxide scale, the corrosion pit on the matrix, and the sulfide scale as a source of fractures.

Author Contributions: X.M. contributed to conceptualization, writing—original draft. S.L. contributed to investigation, formal analysis, funding acquisition. X.X. contributed to resources. C.T. and W.Y. contributed to supervision. J.Q. and W.H. contributed to investigation, formal analysis. J.D. and C.W. contributed to resources and supervision. All authors have read and agreed to the published version of the manuscript.

Funding: This work was supported by the National Science and Technology Major Project (J2019-VI-0006-0120) and National Natural Science Foundation of China (Grant No. 52274330, 52074092).

Institutional Review Board Statement: Not applicable.

Informed Consent Statement: Not applicable.

Data Availability Statement: The original contributions presented in this study are included in this article. Further inquiries can be directed to the corresponding author.

Conflicts of Interest: Author Xinyu Meng was employed by the Central Iron and Steel Research Institute Co., Ltd. and Beijing GAONA Materials and Technology Co., Ltd.; Authors Shaomin Lyu, Xingfei Xie, Chao Tang, Weixue Hou, Chengyu Wang, Jinglong Qu and Jinhui Du were employed by the Beijing GAONA Materials and Technology Co., Ltd. and Sichuan CISRI-GAONA Forging Co., Ltd. Author Wugang Yu was employed by the NCS Testing Technology Co., Ltd. The authors declare that the research was conducted in the absence of any commercial or financial relationships that could be construed as a potential conflict of interest.

References

1. Shi, C.X.; Zhong, Z.Y. Development and Innovation of Superalloy in China. *Acta Met. Sin.* **2010**, *46*, 1281–1288. [CrossRef]
2. Jiang, H.H.; Dong, J.X.; Zhang, M.C.; Yao, Z.H. Development of Typical Hard-to-Deform Nickel-Base Superalloy for Turbine Disk Served Above 800 °C. *Aeronaut. Manuf. Technol.* **2021**, *64*, 62–73.
3. Huang, S.; Sun, R.K.; Wang, L.; Dong, D.Y.; Duan, R.J.; Song, X.; Liu, Y. Microstructure evolution and fracture mechanism of a Fe–Ni–Cr superalloy during various strain rates tensile deformation at elevated temperatures. *J. Mater. Sci.* **2023**, *58*, 5901–5920. [CrossRef]
4. Magazzù, A.; Marcuello, C. Investigation of Soft Matter Nanomechanics by Atomic Force Microscopy and Optical Tweezers: A Comprehensive Review. *Nanomaterials* **2023**, *13*, 963. [CrossRef]
5. Liu, S.; Sun, Y.; Zhai, P.; Fan, P.; Zhang, Y.; Li, M.; Fang, J.; Wu, R.; Cai, Z. Microstructure and Properties of Nickel-Based Gradient Coatings Prepared Using Cold Spraying Combined with Laser Cladding Methods. *Materials* **2023**, *16*, 1627. [CrossRef] [PubMed]
6. Schulz, U.; Menzebach, M.; Leyens, C.; Yang, Y.Q. Influence of substrate material on oxidation behavior and cyclic lifetime of EB-PVD TBC systems. *Surf. Coat. Technol.* **2001**, *146*, 117–123. [CrossRef]
7. Shi, J.; Zhang, T.B.; Sun, B.; Wang, B.; Zhang, X.H.; Song, L. Isothermal oxidation and TGO growth behavior of NiCoCrAlY-YSZ thermal barrier coatings on a Ni-based superalloy. *J. Alloys Compd.* **2020**, *844*, 156093. [CrossRef]
8. Li, M.; Wang, P.; Yang, Y.Q.; Yang, Y.Z.; Pei, H.P.; Wen, Z.X.; Yue, Z.F. Oxidation behavior of a nickel-based single crystal superalloy at 1100 °C under different oxygen concentration. *J. Mater. Sci.* **2022**, *57*, 3822–3841. [CrossRef]
9. Long, H.B.; Mao, S.C.; Liu, Y.N.; Zhang, Z.; Han, X.D. Microstructural and compositional design of Ni-based single crystalline superalloys—A review. *J. Alloys Compd.* **2018**, *743*, 203–220. [CrossRef]
10. Park, S.J.; Seo, S.M.; Yoo, Y.S.; Jeong, H.W. Effects of Al and Ta on the high temperature oxidation of Ni-based superalloys. *Corros. Sci.* **2014**, *90*, 305–312. [CrossRef]
11. Ismail, F.B.; Vorontsov, V.A.; Lindley, T.C.; Hardy, M.; Dye, D. Shollock, Alloying effects on oxidation mechanisms in polycrystalline Co–Ni base superalloys. *Corros. Sci.* **2016**, *116*, 44–52. [CrossRef]
12. Liu, Z.S.; Ding, Q.Q.; Zhou, Q.; Yao, X.; Wei, X.; Zhao, X.B.; Wang, Y.; Zhang, Z.; Bei, H. The effect of oxidation on microstructures of a Ni-based single crystal superalloy during heat-treatment and simulated service conditions. *J. Mater. Sci.* **2023**, *58*, 6343–6360. [CrossRef]
13. Li, S.L.; Qi, H.Y.; Yang, X.G. Oxidation-induced damage of an uncoated and coated nickel-based superalloy under simulated gas environment. *Rare Met.* **2018**, *37*, 204–209. [CrossRef]
14. Iyer, A.H.S. Oxidation Induced Failure of Superalloys: High Temperature Crack Growth and Oxide Scale Properties. Ph.D. Dissertation, Chalmers University of Technology, Gothenburg, Sweden, 2017.
15. Sun, B.; Zhang, T.B.; Song, L.; Zhang, L. Oxidation behavior in static air and its effect on tensile properties of a powder metallurgy EP962NP nickel-based superalloy. *J. Alloys Compd.* **2023**, *934*, 167795. [CrossRef]
16. Li, D.H.; Chen, J.X.; Etim, I.; Liu, Y.; Wu, C.J.; Wang, J.H.; Su, X.P. High temperature oxidation behavior of Ni-based superalloy Nimonic95 and the effect of pre-oxidation treatment. *Vacuum* **2021**, *194*, 110582. [CrossRef]
17. Mahobia, G.S.; Paulose, N.; Singh, V. Hot corrosion behavior of superalloy IN718 at 550 and 650 °C. *J. Mater. Eng. Perform.* **2013**, *22*, 2418–2435. [CrossRef]
18. Wei, C.; Wang, Z.J.; Chen, J.G. Sulfuration corrosion failure analysis of Inconel 600 alloy heater sleeve in high-temperature flue gas. *Eng. Fail. Anal.* **2022**, *135*, 106111. [CrossRef]
19. Birbilis, N.; Buchheit, R.G. Measurement and discussion of low-temperature hot corrosion damage accumulation upon nickel-based superalloy Rene 104. *Metall. Mater. Trans. A* **2008**, *39*, 3224–3232. [CrossRef]
20. Nazmy, M.Y. The effect of environment on the high temperature low cycle fatigue behaviour of cast nickel-base IN-738 alloy. *Mater. Sci. Eng.* **1982**, *55*, 231–237. [CrossRef]
21. Wang, H.; Dong, H.; Cai, Z.W.; Liu, Y.Z.; Wang, W.Z. Fatigue behaviors of a nickel-based superalloy after hot-corrosion: Experiments and peridynamic simulations. *Int. J. Fatigue* **2023**, *180*, 108070. [CrossRef]
22. Chang, W.; Ji, Y.L.; Li, J.P. Application analysis in the development and production of aero-engine materials. *Aviat. Stand-Ardisation Qual.* **2014**, *3*, 3.
23. Xu, W.X.; Xu, W.C. Comparison and understanding of the main changes of GB/T228.1-2021. *Phys. Chem. Test. Phys. Div.* **2022**, *58*, 4.
24. Shi, W.; Zhang, L.; Li, X. Application of GB/T6394-2017 in titanium alloy grain size assessment. *Phys. Chem. Test. Phys. Div.* **2019**, *55*, 5.
25. Gui, Y.T.; Zhao, M.; Jiang, P.R.; Ye, W.; Zhao, J.Q.; Zhao, Y.S.; Qiao, Y.Q.; Wu, S.S.; Yan, Y.W. New insights into effects of Ru on the oxidation behaviour of Ni-based single-crystal superalloys at 1150 °C. *Corros. Sci.* **2023**, *223*, 111464. [CrossRef]
26. Yang, B.S.; Li, B.; Chen, X.X.; Zhang, Y.N.; Li, Y.Z. Influence of temperature on hot corrosion behavior of GH4169 superalloy subjected to Na_2SO_4-NaCl salts attack. *Mater. Chem. Phys.* **2024**, *325*, 129731. [CrossRef]

27. Zheng, L.; Maicang, Z.; Jianxin, D. Hot corrosion behavior of powder metallurgy Rene95 nickel-based superalloy in molten NaCl–Na_2SO_4 salts. *Mater. Des.* **2011**, *32*, 1981–1989. [CrossRef]
28. Jiang, J.F.; Xiao, G.F.; Wang, Y.; Liu, Y.Z. High temperature oxidation behavior of the wrought Ni-based superalloy GH4037 in the solid and semi-solid state. *J. Alloys Compd.* **2019**, *784*, 394–404. [CrossRef]
29. Wo, J.; Pang, H.T.; Wilson, A.S.; Hardy, M. The Isothermal Oxidation of a New Polycrystalline Turbine Disk Ni-Based Superalloy at 800 °C and Its Modification with Pre-oxidation. *Metall. Mater. Trans. A* **2023**, *54*, 1946–1960. [CrossRef]
30. Jiang, R.; Zhang, L.C.; Zhao, Y.; Chen, X.H. Effects of hot corrosion on fatigue performance of GH4169 alloy. *J. Mater. Eng. Perform.* **2021**, *30*, 2300–2308. [CrossRef]
31. Song, Y.D.; Ling, C.; Zhang, L.C.; Li, M.L.; Guo, J.W.; Jiang, R. Research Progress on Hot Corrosion-Fatigue of Aero-engine and Gas Turbine Hot-Section Components. *J. Nanjing Univ. Aeonautics Astronaut.* **2022**, *54*, 771–788.
32. Abbasi, M.; Kim, D.; Shim, J.H.; Jung, W.S. Effects of alloyed aluminum and titanium on the oxidation behavior of INCONEL 740 superalloy. *J. Alloys Compd.* **2016**, *658*, 210–221. [CrossRef]
33. Yu, K.P.; Jiang, H.; Xu, X.Y.; Huang, M.X. Design of corrosion-resistant alloys for preventing oxidation-induced nanoscale Cr-depletion by inclusion engineering. *Mater. Des.* **2024**, *244*, 113146. [CrossRef]
34. Han, S.H.; Choe, B.; Kim, D.; Kim, J.H. The effect of TCP-σ precipitates on surface pitting and cracking in a Ni-based superalloy turbine blade. *Eng. Fail. Anal.* **2024**, *158*, 107989. [CrossRef]
35. Yang, S.Y. Thermodynamic Analysis and Alloy Design of Co-AL-W Based Superalloy. Ph.D. Dissertation, Northeastern University, Shenyang, China, 2012.
36. Douglass, D.L. A critique of internal oxidation in alloys during the post-wagner era. *Oxid. Met.* **1995**, *44*, 81–111. [CrossRef]
37. Andreev, Y.Y. Adsorption equilibrium at the metal-oxide film interface in the oxidation reactions of Ni, Cr, and their alloys. *Russ. J. Phys. Chem.* **2007**, *81*, 967–973. [CrossRef]
38. Tsaur, C.C.; Rock, J.C.; Wang, C.J.; Su, Y.J. The hot corrosion of 310 stainless steel with pre-coated NaCl/Na_2SO_4 mixtures at 750 °C. *Mater. Chem. Phys.* **2005**, *89*, 445–453. [CrossRef]
39. Liu, S.; Feng, J.; Luo, X.; Chen, X. Effect of special grain boundary on hot corrosion path in Incoloy825 alloy. *J. Mater. Sci.* **2022**, *57*, 15560–15580. [CrossRef]
40. Li, P.; Li, T.; Zhao, J.; Pang, S.J. Hot corrosion behaviors of super 304H austenitic stainless steel pre-coated in Na_2SO4–25%NaCl mixture salt film. *J. Iron Steel Res. Int.* **2018**, *25*, 1149–1155. [CrossRef]
41. Smialek, J.L. A deterministic interfacial cyclic oxidation spalling model. *Acta Mater.* **2003**, *51*, 469–483. [CrossRef]
42. Qu, W.; Li, J.; Hill, J.M.; Ivey, D.G. Electrical and microstructural characterization of spinel phases as potential coatings for SOFC metallic interconnects. *J. Power Sources* **2006**, *153*, 114–124. [CrossRef]
43. Birks, N.; Meier, G.; Pettit, F. *Introduction to the High Temperature, Oxidation of Metals*, 2nd ed.; Cambridge University Press: New York, NY, USA, 2006.
44. Xu, C.; Gao, W. Pilling-Bedworth ratio for oxidation of alloys. *Mater. Res. Innov.* **2000**, *3*, 231–235. [CrossRef]
45. He, X.; Li, W.; Kong, D.C.; Zhang, W. The kinetics of pitting corrosion in a defect-contained Hastelloy X alloy fabricated by laser powder bed fusion. *Corros. Sci.* **2024**, *237*, 112321. [CrossRef]
46. Gabb, T.P.; Telesman, J.; Hazel, B.; Mourer, D. The effects of hot corrosion pits on the fatigue resistance of a disk superalloy. *J. Mater. Eng. Perform.* **2010**, *19*, 77–89. [CrossRef]
47. Jack, T.; Gabb, T.P.; Yamada, Y. Fatigue resistance of a hot corrosion exposed disk superalloy at varied test temperatures. *Mater. High Temp.* **2016**, *33*, 517–527.
48. Dong, N. Effects of Alloying Elements on the Formation and Bonding Strength of New Alumina-Forming Austenitic Heat-Resistant Steel/Oxide Scale Interface. Ph.D. Dissertation, Taiyuan University of Technology, Taiyuan, China, 2017.
49. Giggins, C.S.; Pettit, F.S. Oxidation of Ni-Cr-Al alloys between 1000 and 1200 °C. *J. Electrochem. Soc.* **1971**, *118*, 1782. [CrossRef]
50. Perez, T.; Monceau, D.; Desgranges, C. Kinetic oxidation model including the transient regime for a single crystal nickel-based superalloy over the temperature range 750–1300 °C. *Corros. Sci.* **2022**, *206*, 110485. [CrossRef]
51. Young, D. Predicting Internal Oxidation: Building on the Wagner Model. *Mater. Sci. Forum* **2011**, *696*, 1–11. [CrossRef]
52. Park, J.W.; Altstetter, C.J. The diffusion and solubility of oxygen in solid nickel. *Metall. Trans. A* **1987**, *18*, 43–50. [CrossRef]
53. Allison, H.W.; Samelson, H. Diffusion of aluminum, magnesium, silicon, and zirconium in nickel. *J. Appl. Phys.* **1959**, *30*, 1419–1424. [CrossRef]
54. Pettit, F.S. Oxidation mechanisms for nickel-aluminum alloys at temperatures between 900 °C and 1300 °C. *Trans. Metall. Soc. AIME* **1967**, *239*, 1296–1305.
55. Nesbitt, J.A. Predicting Minimum Aluminum Concentrations for Protective Scale Formation on Ni-Base Alloys: II. Cyclic Oxidation. *J. Electrochem. Soc.* **1989**, *13*, 1518. [CrossRef]
56. Zhao, W.; Kang, Y.H.; Orozco, J.M.A.; Gleeson, B.M. Quantitative approach for determining the critical volume fraction for the transition from internal to external oxidation. *Oxid. Met.* **2015**, *83*, 187–201. [CrossRef]

57. Jiang, H.; Dong, J.X.; Zhang, M.C.; Guo, W.M. Microstructural Evolution and Oxidation Behavior of Alloy Ni-13Mo-13Cr-9W-3Fe-3Ti-2Al during Isothermal Exposure at 900 °C. *Metall. Mater. Trans. A* **2019**, *50*, 4331–4343. [CrossRef]
58. Waeytens, M.; Syed, A.U.; Roberts, T.; Martinez, F.D. A microscopy study of nickel-based superalloys performance in type I hot corrosion conditions. *Mater. High Temp.* **2023**, *40*, 272–282. [CrossRef]

Disclaimer/Publisher's Note: The statements, opinions and data contained in all publications are solely those of the individual author(s) and contributor(s) and not of MDPI and/or the editor(s). MDPI and/or the editor(s) disclaim responsibility for any injury to people or property resulting from any ideas, methods, instructions or products referred to in the content.